Energy & Environmental Science

ROYAL SOCIETY OF CHEMISTRY

PAPER

View Article Online
View Journal

Cite this: DOI: 10.1039/d4ee00881b

Facet-governed Zn homoepitaxy *via* lattice potential regulation†

Xianzhong Yang, ‡[ab] Yan Lu,‡[c] Zhetong Liu,‡[d] Haoqing Ji,[a] Ziyan Chen,[a] Jun Peng,[e] Yiwen Su,[a] Yuhan Zou,[a] Chao Wu,[b] Shixue Dou,[b] Peng Gao, *[d] Zaiping Guo *[f] and Jingyu Sun *[a]

Received 26th February 2024,
Accepted 13th June 2024

DOI: 10.1039/d4ee00881b

rsc.li/ees

The irreversibility of the Zn anode stemming from disordered Zn deposition and rampant hydrogen evolution has been a formidable challenge, impeding the practical advancement of aqueous Zn-ion batteries. Directing the epitaxial deposition of polycrystalline Zn at the anode/electrolyte interface is appealing to address the obstacle, but remains poorly explored. Here, a comprehensive strategy by employing facet-governed homoepitaxy of polycrystalline Zn *via* lattice potential regulation is reported. The crystallinity of the Zn substrate could be significantly improved during the growth of a prototype fluoride-contained overlayer by chemical vapour deposition. This treatment establishes a periodic lattice potential field for Zn deposition. The introduction of an overlayer promotes the uniform nucleation of Zn at the infancy stage of electrodeposition. To counteract the tip effect of Zn growth, an ionic liquid is concurrently employed to alleviate Zn^{2+} accumulation throughout cation adsorption, fostering stable orientational deposition. Such an additive can also reduce water activity, effectively inhibiting hydrogen evolution. The thus-derived Zn anodes demonstrate decent durability even at a low N/P ratio. This work unlocks a new opportunity for guiding epitaxial Zn deposition toward pragmatic Zn anodes.

Broader context

In the realm of aqueous Zn-ion batteries, the precise regulation of Zn deposition along specific crystallographic facets, such as (002), (100), or (101), emerges as a promising strategy to mitigate dendrite growth. Nonetheless, the intrinsic polycrystalline nature of commercial Zn foil impedes the seamless integration between induced orientational deposition and the substrate. Over prolonged cycling periods, the accumulation of structural distortion persists, giving rise to dendrite growth. In this study, we introduce a distinctive approach, focusing on directing facet-governed Zn homoepitaxy of polycrystalline Zn through lattice potential regulation. The crystallinity of the Zn substrate undergoes significant enhancement through the chemical vapor deposition method, involving the growth of a fluoride-containing overlayer. This process effectively establishes a periodic lattice potential field for Zn homoepitaxial deposition. The overlayer promotes uniform Zn nucleation during early electrodeposition stages. To counteract Zn growth challenges, an ionic liquid is used, alleviating Zn^{2+} accumulation and fostering stable deposition. Additionally, the additive reduces water activity, inhibiting hydrogen evolution. This work delineates an approach for guiding Zn homoepitaxial deposition of polycrystalline Zn, thereby confronting inherent challenges and augmenting advancements in next-generation energy storage technologies.

Introduction

The burgeoning global energy storage market is propelling considerable demand for advanced batteries featuring heightened performance and economic viability, surpassing the constraints inherent in contemporary Li-based technology.[1] Within this context, aqueous Zn-ion batteries (AZIBs) have emerged as an appealing alternative because of their collective merits, encompassing high theoretical capacity, abundant resources, and intrinsic safety.[2,3] Nevertheless, the pragmatic application of AZIBs is still handicapped by thorny issues associated with the Zn anode,[4] specifically in relation to dendrite growth and hydrogen evolution. The proclivity of Zn

[a] College of Energy, Soochow Institute for Energy and Materials Innovations, Key Laboratory of Advanced Carbon Materials and Wearable Energy Technologies of Jiangsu Province, Soochow University, Suzhou 215006, P. R. China. E-mail: sunjy86@suda.edu.cn
[b] Institute of Energy Materials Science, University of Shanghai for Science and Technology, Shanghai 200093, P. R. China
[c] Department of Physics, Nanchang University, Nanchang 330031, P. R. China
[d] Electron Microscopy Laboratory, International Center for Quantum Materials, School of Physics, Peking University, Beijing 100871, P. R. China. E-mail: pgao@pku.edu.cn
[e] Center for Hybrid Nanostructures, Universität Hamburg, Hamburg 22761, Germany
[f] School of Chemical Engineering, The University of Adelaide, Adelaide, SA 5005, Australia. E-mail: zaiping.guo@adelaide.edu.au

† Electronic supplementary information (ESI) available. See DOI: https://doi.org/10.1039/d4ee00881b

‡ These authors contributed equally to this work.

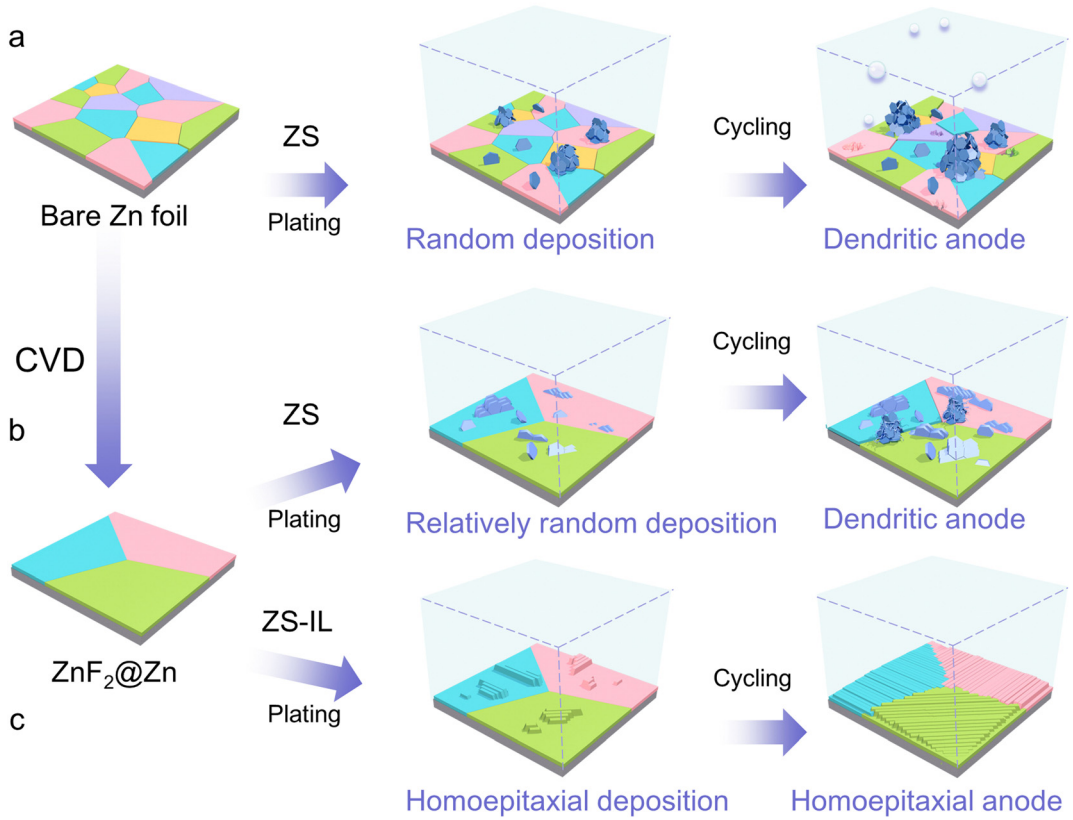

Scheme 1 Schematic diagram showing Zn deposition behaviour ultimately dictated by the dual-modulation strategy. (a) Zn deposition behavior of the bare Zn anode in the ZS electrolyte. (b) Zn deposition behavior of the ZnF_2@Zn anode in the ZS electrolyte. (c) Zn deposition behavior of the ZnF_2@Zn-IL anode in the ZS-IL electrolyte.

metal to generate irregular dendritic forms within the $ZnSO_4$ (ZS) electrolyte (Scheme 1a) would result in diminished Coulombic efficiency (CE), reduced capacity, and short circuits.[5] The hydrogen evolution normally induces increased polarization and marked volume expansion of batteries. Even worse, the dendrite formation and hydrogen evolution mutually foster each other, culminating in the premature failure of the AZIBs.[6] In light of these caveats, it becomes imperative to devise effective solutions to realize a reversible and durable Zn anode.

Extensive efforts have thus far been devoted to ameliorating the long-standing issues of the Zn anode, mainly encompassing the implementation of artificial interphase layers (AILs),[7] utilization of electrolyte additives,[8] construction of functional separators,[9] and design of electrode architectures.[10,11] It is worth noting that a sole regulating tactic poses certain limitations. For instance, AILs are susceptible to damage during long-term cycling,[12] thereby compromising their protective efficacy. The architecture design of the electrode fails to isolate the direct contact between Zn and the electrolyte, which inevitably initiates the onsets of side reactions. In this sense, there arises a critical need for a comprehensive strategy that effectively harnesses the cumulative benefits to develop advanced Zn anodes.

Manipulating the crystallographic aspects represents a promising avenue to achieve a uniform and densely packed arrangement of Zn islands,[13,14] which would mitigate the dendrite formation. The pioneering study in 2019 on Zn heteroepitaxy *via* graphene indeed catalyzed considerable interest in regulating the orientational deposition of Zn.[15] Guo's group introduced a covalent organic framework film to guide the orientational Zn deposition along Zn(002).[16] Additionally, Chen *et al.* successfully transformed commercial Zn foils into (002)-textured Zn, thus enabling good reversibility.[17] In parallel efforts, Lu and Zhang's group respectively reported the regulation of orientational deposition along Zn(101).[18,19] Although inducing Zn(002) or Zn(101) dominated growth over Zn foils has showcased certain merits in promoting electrochemical performances, there remains a neglected fact that the thus-derived oriented crystals might not seamlessly integrate with the underlying polycrystalline Zn substrate.[20] This lack of coherent merge might cause deviations from the original lattice growth and the accumulation of lattice distortion, potentially leading to the failure of orientational deposition.[19,21] Along this line, if selective epitaxial growth of Zn can be directly realized based on the polycrystalline Zn substrate, the challenge could be well circumvented. Such a highly sought-after goal lies in manipulating homoepitaxial Zn deposition over polycrystalline Zn foils. Nonetheless, the related investigation has been rarely reported, with the underlying mechanism remaining elusive to date.

In this contribution, we develop an innovative dual-modulation strategy by combining an *in situ* grown prototype overlayer (ZnF_2@Zn) with a designed ionic liquid (1,3-dimethylimidazolium

iodide, MMImI) electrolyte additive (ZS-IL) to enable a reversible Zn anode. The zincophilic ZnF_2 generated *via* chemical vapor deposition (CVD) plays a crucial role in offering uniform nucleation sites (Scheme 1b). More importantly, the thermal annealing process during CVD could substantially improve the crystallinity of the Zn foil substrate, rendering a periodic lattice electrostatic potential. Such a periodic potential further guides incoming Zn adatoms on the surface to align with the atomic patterns of the Zn substrate. Simultaneously, the adsorption of $MMIm^+$ onto the Zn surface can inhibit the accumulation of Zn ions at the tip of electrodeposited Zn islands, thereby promoting a homogeneous deposition (Scheme 1c). In essence, this collaborative strategy contributes to realizing homoepitaxial Zn over a polycrystalline Zn substrate. The facet-governed growth is in favor of achieving a smooth Zn layer, which advances the Zn anode with favorable plating/stripping rates and capacities. As a result, the symmetric cell demonstrates impressive durability across diversified test conditions, including prolonged cycling for 6500 h at 1.0 mA cm^{-2}/1.0 mA h cm^{-2} and 500 h at 30.0 mA cm^{-2}/10.0 mA h cm^{-2}. When paired with a $Zn_xV_2O_5{\cdot}H_2O$ (ZVO) cathode, the full battery harvests an extended lifespan exceeding 11000 cycles.

Results and discussion

Synthesis and characterization of ZnF_2@Zn

Each grain of polycrystalline Zn substrate exposes a single crystal facet. To illustrate the homoepitaxy concept for polycrystalline Zn, Fig. 1a presents the atomic growth model along three typical crystal facets: Zn(002), (100), and (101). The epitaxial layer and the substrate exhibit a perfect lattice match (Fig. S1, ESI†), which fosters coherent growth. The CVD growth of the ZnF_2 overlayer and the incorporation of IL are crucial to ensure the stability of this homoepitaxy process. Despite the fact that the application of ZnF_2 in Zn anode protection has been extensively studied, it is acknowledged that the mechanism was mainly centered on the perspective of AILs.[22,23] Our study probes the role of ZnF_2 in dictating Zn electrodeposition from an innovative standpoint. In fact, during the CVD growth of ZnF_2 at elevated temperature (Fig. S2, ESI†), the Zn substrate itself also undergoes noticeable crystallographic changes, which will have a profound impact on the plating/stripping of Zn. Upon CVD growth, the surface of Zn foil turns a light grey color to the naked eye (Fig. S3a and b, ESI†), implying the successful coating of ZnF_2. Notably, a large-scale ZnF_2@Zn sample featuring a size of 20 cm × 10 cm could be readily synthesized using a 4-inch tube furnace (Fig. S3c, ESI†), holding potential for scalable production in a cost-effective manner. Based on a systematic parameter investigation, 280 °C was selected as the optimal growth temperature for ZnF_2@Zn (Fig. S4, ESI†). X-ray photoelectron spectroscopy (XPS) results bear out the existence of both Zn and F elements on the ZnF_2@Zn surface (Fig. S5, ESI†). The crystallographic information of ZnF_2 was revealed by X-ray diffraction (XRD) (Fig. 1b; Fig. S6, ESI†). Two diffraction peaks located at 26.9° and 34.5° can be assigned to the (110) and (101) planes of ZnF_2,

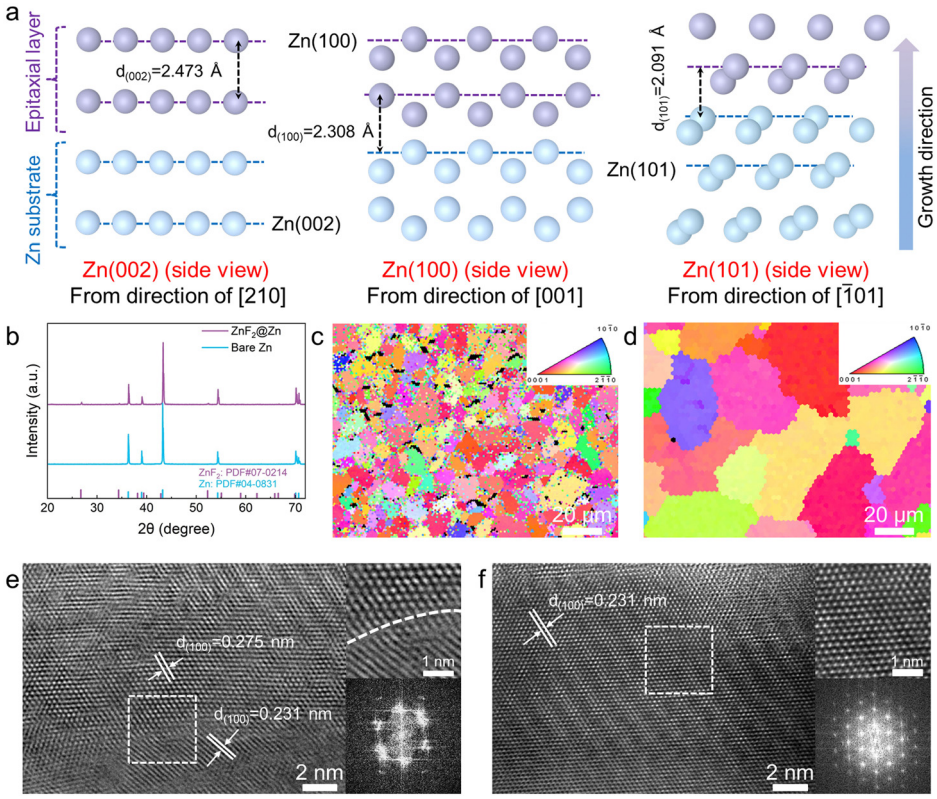

Fig. 1 Characterization of bare Zn and ZnF_2@Zn. (a) Homoepitaxy diagram of typical Zn crystal facets. (b) XRD patterns of bare Zn and ZnF_2@Zn. EBSD mapping of (c) bare Zn and (d) ZnF_2@Zn. High resolution TEM images of (e) bare Zn and (f) ZnF_2@Zn.

respectively. By the introduction of the hydrophilic ZnF_2 coating, there is an apparent decrease in the contact angle of Zn foil (from 94.4° to 75.5°, Fig. S7, ESI†), which might be beneficial for promoting uniform ion transport. Note that the contact angle remains 95.3° upon a blank CVD process under identical conditions without the NH_4F precursor, excluding the influence of thermal annealing on wettability enhancement.

The surface morphology of bare Zn and ZnF_2@Zn was inspected by scanning electron microscopy (SEM). Several irregular protuberances could be observed on the bare Zn surface, which might result in dendrite formation. A wealth of distributed cracks become evident on ZnF_2@Zn, which are related to the grain boundaries arising from thermal annealing (Fig. S8, ESI†). The high-magnification SEM image reveals that the ZnF_2 overlayer predominantly exists in the form of nanoparticles (Fig. S8d, ESI†). At lower reaction temperatures (<250 °C), annealing-induced atomic movement is not pronounced, resulting in the absence of obvious grain boundaries (Fig. S9, ESI†). In contrast, elevated temperatures (>350 °C) could lead to surface breakage of Zn foil. In addition, varying the growth duration affects the grain size, with a minimal impact on the microstructure of ZnF_2@Zn at a suitable temperature (Fig. S10, ESI†). Symmetric cell tests further confirm the suitability of the selected growth procedure (Fig. S11, ESI†). To elucidate the crystallographic change upon CVD, electropolishing was carried out, followed by a standard metallographic characterization procedure.[24] As shown in the optical microscopy images (Fig. S12a and b, ESI†), both bare Zn and ZnF_2@Zn present spliced grains, with the average size of the latter significantly increasing from ~5 to 55 um. The side-view optical micrograph reveals that approximately 50 μm of Zn was removed during the electropolishing process (Fig. S12c and d, ESI†). Therefore, the crystal facets observed are attributed to Zn itself rather than ZnF_2. These observations are further verified by SEM (Fig. S13, ESI†). Accordingly, electron backscatter diffraction (EBSD) was employed to visualize the crystal orientations of bare Zn and ZnF_2@Zn.[25] As depicted in Fig. 1c, the EBSD mapping of bare Zn displays abundant noise signal owing to the irregular crystal structure.[26] In stark contrast, the noise signal is markedly diminished in the case of ZnF_2@Zn (Fig. 1d). Therefore, the thermal-driven atomic reconstruction of Zn can effectively eradicate unstable grain boundaries and defects, expecting improved electrochemical performances of the Zn electrode.

High-resolution imaging with the aid of spherical-aberration corrected transmission electron microscopy (TEM) was performed to scrutinize the lattice structure evolution of Zn after the CVD process. The TEM samples were prepared *via* focused ion beam (FIB) cutting and thinning, as demonstrated in Fig. S14 (ESI†). The energy-dispersive X-ray spectroscopy (EDS) mapping conducted in the high-angle annular dark field mode reveals the uneven distribution of Zn and F elements on the topmost surface of ZnF_2@Zn (Fig. S15, ESI†). This observation implies that fluorination predominantly occurred at a depth of approximately 30 nm. As for bare Zn, TEM images depict numerous lattice defects (Fig. 1e; Fig. S16, ESI†), including the stacking fault and lattice tortuosity.[26] In particular, the atomic-scale image with its fast Fourier transform (FFT) pattern illustrates the distortion of the lattice structure (Fig. 1e inset). Moreover, the Zn (100) plane exhibits lattice expansions in certain regions, with the interplanar spacing reaching ~0.275 nm. Such an expansion represents a 13% increase relative to the standard crystal plane, indicative of marked lattice deformations. Encouragingly, ZnF_2@Zn showcases a highly ordered and neatly arranged lattice pattern, as shown in Fig. 1f and Fig. S17 (ESI†). Collectively, the CVD process not only generates a zincophilic ZnF_2 overlayer but also induces a thermal-driven rearrangement of atoms. This accordingly contributes to the elimination of lattice defects, reduction of grain boundaries, and formation of relatively perfect grain regions. The noticeable improvement of the crystal quality would exert a key impact on the Zn plating/stripping process.

Modulation of the ZS-IL electrolyte

Along with the designed ZnF_2 overlayer, an electrolyte additive was introduced to synchronously regulate the behavior of Zn plating/stripping. ILs have been widely investigated as electrolyte additives to inhibit dendrite proliferation and ameliorate side reactions.[27] Both the cationic and anionic groups in ILs are conducive to modulating the Zn interfacial chemistry during cycling.[28,29] In this context, MMImI was selected to modulate the Zn electrodeposition at the interface. The selection criteria are discussed in the following section. Note that MMImI can readily dissolve into the typical ZS electrolyte (Fig. S18, ESI†). To gauge the influence of additive dosage on the reversibility of the Zn electrode, the electrochemical performances of symmetric cells equipped with different concentrations were examined (Fig. S19, ESI†). The optimized choice was found to be 0.1 M MMImI added to the ZS electrolyte (ZS-IL).

Molecular dynamics (MD) simulations were carried out to gain theoretical insight into the solvation structure of ZS and ZS-IL. As for the ZS, the snapshot (Fig. 2a) and radial distribution function (RDF, Fig. 2b) manifest that Zn^{2+} is solvated by 5.4 H_2O molecules and 0.8 SO_4^{2-} on average in the first solvation shell, denoted as $Zn^{2+}[H_2O]_{5.4}[SO_4^{2-}]_{0.8}$. Upon dosing MMImI into ZS (Fig. 2c and d; Fig. S20, ESI†), the coordination number of H_2O exhibits a slight reduction from 5.4 to 4.9, which is concomitant with an elevated coordination number of SO_4^{2-} from 0.8 to 1.1. Moreover, a relatively weak coordination with a coordination number of 0.2 could be observed between Zn^{2+} and I^-. These simulation results render ZS-IL to show a ternary solvation structure denoted as $Zn^{2+}[H_2O]_{4.9}[SO_4^{2-}]_{1.1}[I^-]_{0.2}$. The solvation of Zn^{2+} was further revealed by nuclear magnetic resonance (NMR) spectroscopy. As shown in Fig. 2e, the ^2H signal in D_2O (4.701 ppm) experiences a downfield shift to 4.714 ppm in ZS, implying the involvement of free water molecules in the solvation structure of Zn^{2+}. As for the ZS-IL electrolyte, the ^2H signal subtly shifts to 4.712 ppm, indicative of the slight liberation of water molecules from the solvated Zn^{2+} shell. The simulation results indicate that the presence of an IL only marginally improves the solvation structure of Zn^{2+}. Complementary to MD simulations and NMR spectroscopic study, Raman spectra were collected to discern the evolution of H-bonds in different electrolytes. Fig. 2f and Fig. S21 (ESI†)

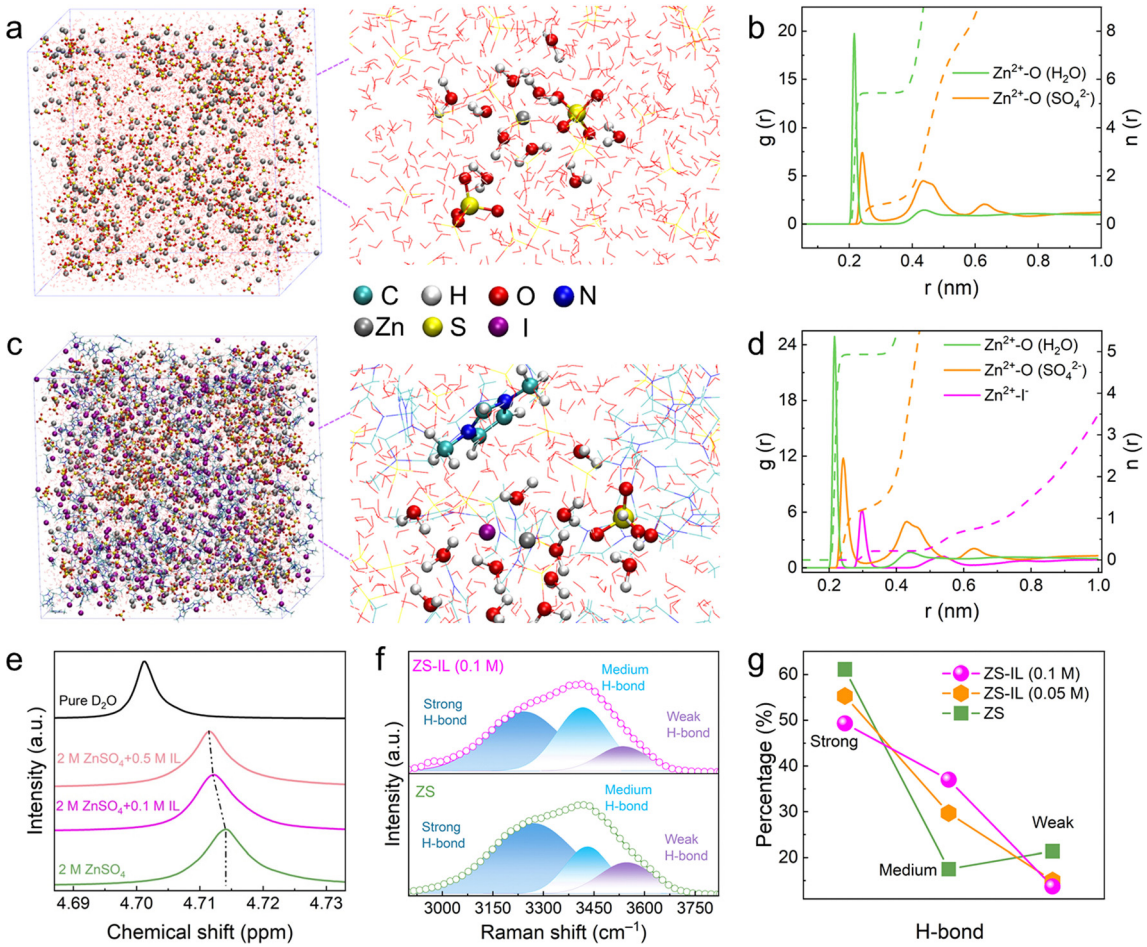

Fig. 2 Characterization of ZS and ZS-IL electrolytes. The MD snapshots of (a) the ZS electrolyte and (c) the ZS-IL electrolyte. RDF and coordination number of (b) the ZS electrolyte and (d) the ZS-IL electrolyte. (e) ^{2}H NMR spectra. (f) Raman spectra of the –OH band. (g) Statistical trends of the three kinds of H-bonds.

show the typical Raman signals of strong (~3250 cm^{-1}), medium (~3430 cm^{-1}), and weak H-bonds (~3550 cm^{-1}).[30] Fig. 2g summarizes the distribution of H-bonds within different electrolytes. Obviously, with the IL addition, the contributions for strong H-bond gradually decrease while those of the medium H-bond increase. This transition has the potential to decrease the interaction between solvated Zn^{2+} and free water molecules, thereby facilitating ion transport. Collectively, these results confirm the slightly improved solvation structure and significantly weakened H-bond, with the potential to suppress hydrogen evolution and accompanied side reactions.

Facet-governed Zn homoepitaxy

The plating/stripping of Zn primarily takes place at the electrode/electrolyte interface. To comprehensively understand the impact of the electrolyte composition and electrode surface chemistry on Zn deposition, a spectrum of microscopic characterization studies was employed. Specifically, the Zn nucleation and growth dynamics under the modulation of ZnF_2@Zn and the IL were intuitively visualized by *in situ* optical microscopy. In terms of the bare Zn electrode paired with the ZS electrolyte (bare Zn–ZS), irregular protuberances emerge sporadically on the electrode surface (Fig. 3a; Fig. S22a, ESI†). This phenomenon becomes pronounced with a lengthy deposition time, ultimately culminating in dendrite formation. In the case of the ZnF_2@Zn system (ZnF_2@Zn–ZS), the deposited Zn exhibits a relative uniformity without conspicuous dendrites, suggestive of a dense nucleation process (Fig. 3b; Fig. S22b, ESI†). In contrast, a homogeneous deposition could be observed when both the ZnF_2@Zn electrode and ZS-IL electrolyte were employed (ZnF_2@Zn-IL), which is featured by a minimal deposition thickness (Fig. 3c; Fig. S22c, ESI†). To perform a comprehensive analysis of the electrodeposition landscape in these systems, digital photos and SEM images were further acquired. It is evident that the Zn growth in bare Zn–ZS is extremely irregular (Fig. 3d; Fig. S23a, ESI†). The surface remains incompletely covered even after deposition at a capacity of 10 mA h cm^{-2}. Upon ZnF_2 coverage, the electrodeposited Zn exhibits a denser morphology (Fig. 3e). Although partial deposition orientation can be achieved after electroplating for a small capacity (0.2 mA h cm^{-2}), the grown Zn displays gradual disorderliness with increasing deposition amount owing to the mass transfer influence within the pure ZS electrolyte.[31] The dendritic emergence after extensive deposition indeed

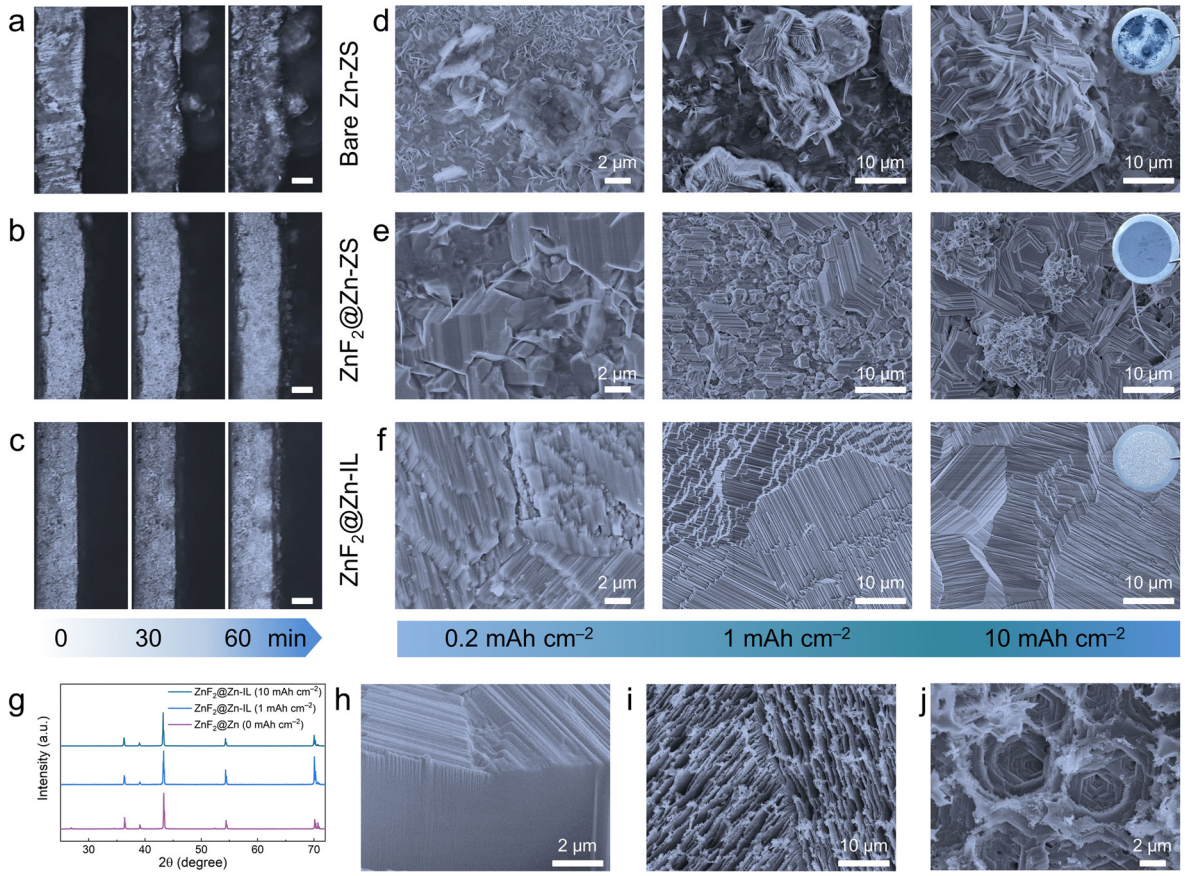

Fig. 3 Characterization of plating/stripping patterns. *In situ* optical microscopy visualization of Zn plating: (a) bare Zn–ZS, (b) ZnF_2@Zn–ZS, and (c) ZnF_2@Zn-IL. Scale bars: 50 μm. Top-view SEM images of Zn anodes with different deposition capacities: (d) bare Zn–ZS, (e) ZnF_2@Zn–ZS, and (f) ZnF_2@Zn-IL. Inset: digital photograph of electrodeposited Zn electrodes. (g) XRD patterns of ZnF_2@Zn electrodes before and after electrodeposition. (h) Side-view FIB-SEM image of the ZnF_2@Zn electrode with 1 mA h cm^{-2} Zn deposition. (i) Top-view SEM image of the ZnF_2@Zn electrode with 10 mA h cm^{-2} Zn stripping. (j) Top-view SEM image of a (002) domain with 10 mA h cm^{-2} Zn stripping.

explains why the deposited Zn loses the metallic luster (Fig. S23b, ESI†). In this context, the metallic luster typically stems from a smooth and uniform surface that reflects light in a consistent manner. Dendritic structures with rough and irregular surfaces scatter light from all directions, resulting in a dull appearance.

To realize a lustrous electrodeposited surface, it is essential to control the deposition conditions to enable a dendrite-free texture. Encouragingly, in the ZnF_2@Zn-IL system, Zn electrodes exhibit a metallic luster at all deposited capacities, as presented in Fig. S23c (ESI†). Our exhaustive SEM observations further confirm the regular arrangement of Zn. At a low deposition capacity of 0.2 mA h cm^{-2} (Fig. 3f, left panel), the Zn islands are uniformly aligned, with each exhibiting a distinct orientation within its grain. Some observations even reveal the growth progression from the interior of the Zn substrate toward the exterior (Fig. S24, ESI†), highlighting the coherent growth patterns resulting from homoepitaxial growth.[32,33] It is noteworthy that the ultra-thin ZnF_2 overlayer almost detached after the initial deposition, leaving only a small residue of nanoparticles on the Zn island surface. As the deposition capacity increases (1.0 mA h cm^{-2}), isolated islands within a grain progressively coalesce (Fig. 3f, middle panel; Fig. S25, ESI†). Remarkably, the electrode exhibits analogous grain dimensions both before and after electrodeposition, providing further evidence of epitaxial growth. High-magnification SEM images of electrodeposited Zn within several representative grains were further collected (Fig. S26, ESI†), revealing Zn deposition along (002) and other crystal facets governed by the underlying substrate. Such a highly orientational deposition stemming from the homoepitaxy of Zn renders a uniform and dense morphology. These findings demonstrate that homoepitaxy along the grain of the Zn electrode is achievable merely when synergistically employing ZnF_2@Zn and IL. The grain dictating morphology could be still preserved even at an elevated deposition capacity of 10 mA h cm^{-2} (Fig. 3f, right panel), which unequivocally demonstrates the impressive stability of this homoepitaxial mode.

There is no perceptible change in the XRD patterns of the Zn electrode at different deposited capacities (Fig. 3g), manifesting the consistency between electrodeposited Zn and the original crystal facet. As shown in Fig. 3h and Fig. S27 (ESI†), cross-sectional FIB-SEM images of Zn electrodes after electrodeposition offer supplementary evidence of the seamless merging status

either within the same crystallographic grain or at the grain boundaries.[21] Taken together, these results corroborate the homoepitaxial deposition of Zn co-modulated by an AIL and electrolyte additive. In addition to uniform deposition, consistent stripping also plays a pivotal role in sustainable Zn cycling.[14] Further microscopic evidence suggests that the stripping processes are also harnessed along the basal Zn facets (Fig. 3i; Fig. S28 and S29, ESI†). Specifically, the Zn(002) region is stripped to form hexagonal voids, which can be evenly "refilled" during subsequent deposition stages (Fig. 3j). Such a desirable feature would contribute to improved structural integrity and enhanced electrochemical performance.

Electrochemical performance of ZnF_2@Zn-IL

Nyquist profiles of Zn symmetric cells were recorded to determine the charge-transfer resistance (R_{ct}, Fig. S30, ESI†). As expected, the ZnF_2@Zn-IL module exhibits the lowest R_{ct} in comparison with those of the bare Zn–ZS and ZnF_2@Zn–ZS counterparts, signifying a synergistic impact of ZnF_2@Zn and the IL. The enhanced kinetics could be attributed to the high electrolyte conductivity (130 mS cm^{-1}, Fig. S31, ESI†) and low desolvation energy of Zn^{2+} (37.0 kJ mol^{-1}) in the ZnF_2@Zn-IL system (Fig. 4a). The desolvation energy was obtained by fitting variable-temperature impedance data (Fig. S32, ESI†) employing the Arrhenius equation.[34,35] A potentiostatic current–time transient curve was recorded to probe the influences of ZnF_2@Zn-IL on Zn nucleation and growth (Fig. 4b). As for the bare Zn–ZS symmetric cell, the continuous increase of current density suggests an expansion of effective electrode area, primarily stemming from the dendrite formation. In contrast, the ZnF_2@Zn-IL symmetric cell experiences a fast nucleation and growth process during the initial 20 seconds, followed by a reverse current response. Such a slight decrease mainly results from the overlap of Zn islands, offering further evidence for the homoepitaxial deposition of Zn. In addition, the linear sweep voltammetry test in Na_2SO_4 solution demonstrates a lower potential of the ZnF_2@Zn-IL as compared to bare Zn–ZS at 10.0 mA cm^{-2} (Fig. S33, ESI†), indicating a sluggish hydrogen evolution rate. Tafel curve analysis shows a slower corrosion current density (Fig. 4c), verifying the inhibitory effect on the corrosion reaction.

Cyclic voltammetry (CV) was carried out to investigate the electrodeposition behavior of Zn in Zn‖Ti asymmetric cells, as

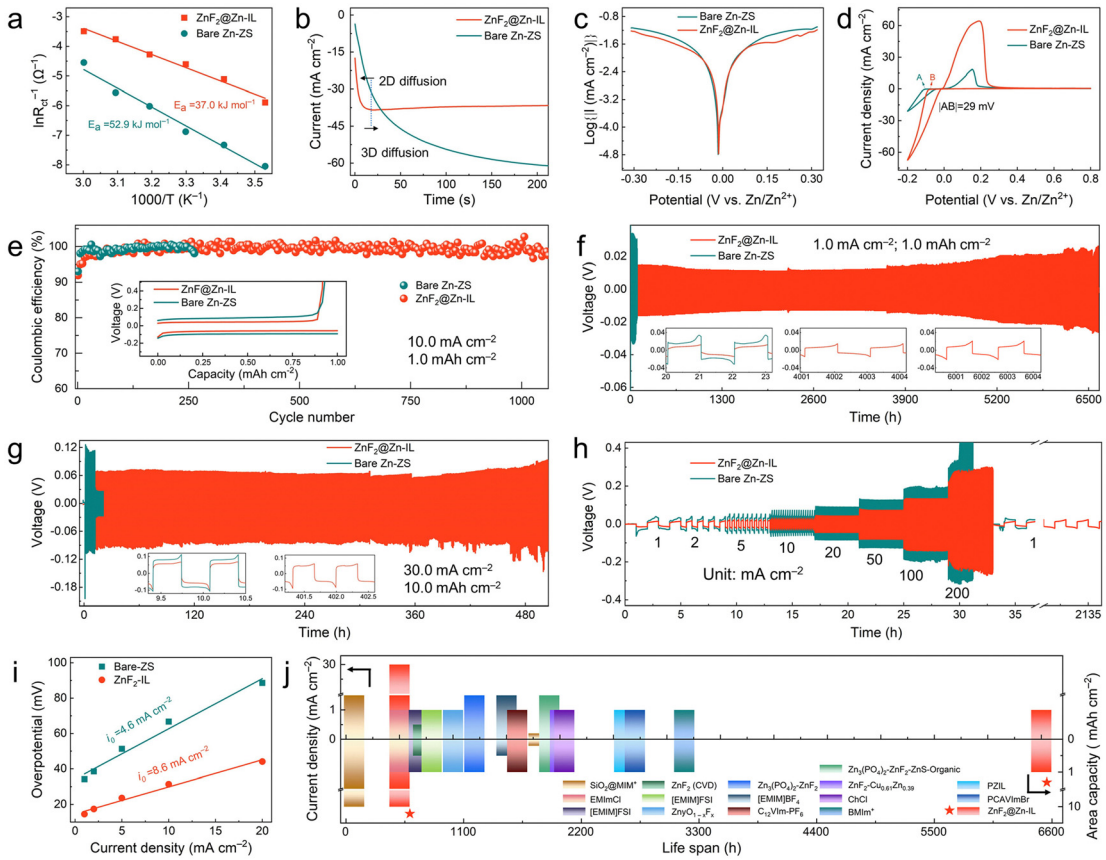

Fig. 4 Electrochemical performances. (a) Arrhenius curves and fitted activation energies for the ZnF_2@Zn-IL and bare Zn–ZS. (b) Chronoamperometry curves of ZnF_2@Zn-IL and bare Zn–ZS symmetric cells at a constant potential of −150 mV. (c) Tafel curves of symmetric cells. (d) CV profiles of ZnF_2@Zn-IL‖Ti and bare Zn–ZS‖Ti asymmetric cells. (e) CE of Zn plating/stripping for Zn‖Ti cells. Inset: corresponding voltage profiles at the first cycle. Long-term galvanostatic cycling of ZnF_2@Zn-IL and bare Zn–ZS symmetric cells at (f) 1.0 mA cm^{-2}/1.0 mA h cm^{-2} and (g) 30.0 mA cm^{-2}/10.0 mA h cm^{-2}. Inset: detailed voltage profiles at specific cycling duration. (h) Rate performances of ZnF_2@Zn-IL and bare Zn–ZS symmetric cells at various current densities and a capacity of 1.0 mA h cm^{-2}. (i) Exchange current density plots. (j) Lifespan comparison between this work and recent studies using ZnF_2 or ILs.

depicted in Fig. 4d. The ZnF_2@Zn-IL‖Ti cell exhibits lower nucleation overpotential and higher current density as compared to those of bare Zn–ZS‖Ti cell, elucidating the existence of more active nucleation sites.[36] CE is a key parameter in assessing the reversibility and durability of Zn plating/stripping. As shown in Fig. 4e, the ZnF_2@Zn-IL‖Ti cell harvests a lower initial overpotential and an average CE value of 99.4% over 1100 cycles, while the bare Zn–ZS‖Ti cell encounters a short circuit issue merely after 250 cycles (Fig. S34a and b, ESI†). Similar trends could also be observed when cycled under harsh conditions of 20.0 mA cm^{-2}/5.0 mA h cm^{-2} (Fig. S34c, ESI†), implying the substantially enhanced sustainability.

To evaluate the efficacy of integrating ZnF_2@Zn and the IL for stabilizing the Zn anode, exhaustive galvanostatic charge/discharge (GCD) tests of symmetric cells were performed across various current densities and areal capacities. The bare Zn–ZS symmetric cell could only run for 40 h under moderate conditions of 1.0 mA cm^{-2}/1.0 mA h cm^{-2} (Fig. 4f), with a considerable voltage hysteresis of 67 mV. In contrast, the ZnF_2@Zn-IL symmetric cell exhibits a stable voltage profile with a reduced voltage hysteresis (24 mV) and an extended lifespan of over 6500 h. Of note, there is a gradual increase in voltage hysteresis after cycling for over 3000 h, predominantly attributed to partial electrolyte loss and minor side reactions.[37] The ZnF_2@Zn-IL cell can also maintain favorable performances even under stringent conditions, including 30.0 mA cm^{-2}/10.0 mA h cm^{-2} (500 h, Fig. 4g) and 40.0 mA cm^{-2}/4.0 mA h cm^{-2} (185 h, Fig. S35, ESI†). The rate capability evaluation of symmetric cells provides further verification of the improved electrochemical behaviour induced by the ZnF_2 coating and IL modification. As the current density increases from 1.0 to 200.0 mA cm^{-2}, consistently lower voltage hysteresis could be gained in the ZnF_2@Zn-IL cell, whereas the bare Zn–ZS cell encounters short-circuits within 30 h (Fig. 4h; Fig. S36, ESI†).

The exchange current density (i_0), representing the rate of the redox reaction, could be derived using the equation: $i = i_0\frac{ZF}{RT}(\varphi_e - \varphi_0) \approx i_0\frac{ZF}{RT}\frac{\eta_t}{2}$. Here, i, i_0, Z, F, R, T, φ_e, φ_0, and η_t is the operating current density, exchange current density, number of electrons involved in the reaction, Faradaic constant, ideal gas constant, ambient temperature, equilibrium overpotential, original potential, and total overpotential, respectively.[38] As presented in Fig. 4i, the deduced i_0 value of ZnF_2-IL (8.6 mA cm^{-2}) is obviously larger than that of bare Zn–ZS (4.6 mA cm^{-2}), confirming the enhanced reaction kinetics for Zn deposition. While the bare Zn–ZS system harnesses a large electrode surface area owing to dendrite growth, the accumulation of surface by-products tends to impede the redox reaction to some extent. Furthermore, the partial involvement of I^- in the solvation structure of Zn^{2+} diminishes the interaction between solvated Zn^{2+} and water molecules, thus enhancing the ion conductivity. These factors, combined with the lower desolvation energy barrier for the ZnF_2@Zn-IL, contribute to the accelerated reaction kinetics. Even at elevated current densities of 100.0 mA cm^{-2} and 200.0 mA cm^{-2}, the ZnF_2@Zn-IL cell also demonstrates impressive stability, enduring 8250 and 1550 cycles, respectively (Fig. S37, ESI†). Morphological analysis further suggests the epitaxial deposition along the grain even at 100.0 mA cm^{-2} (Fig. S38, ESI†). As summarized in Fig. 4j, the performance of the ZnF_2@Zn-IL system outperforms other reported IL additives or ZnF_2 AIL counterparts,[29,39–57] indicating its potential application in the pragmatic Zn anode (Table S1–S3, ESI†).

The combination of ZnF_2@Zn and ILs can effectively reduce the nucleation overpotential (Fig. S39, ESI†), thus promoting uniform and dense nucleation by lowering the related energy barrier.[2] SEM observations of the cycled bare Zn electrode display the formation of dendrites and deep pits, whereas highly oriented Zn is uniformly covered on the electrode surface of the ZnF_2@Zn-IL system (Fig. S40, ESI†). Optical surface profilometry imaging reveals that the electrode surface of the ZnF_2@Zn-IL system exhibits declined height fluctuation as compared to the bare Zn–ZS system upon cycling (Fig. S41, ESI†). In addition, the Zn^{2+} transference number evaluation of ZnF_2@Zn-IL also demonstrates a noticeable amplification from 0.19 to 0.45 (Fig. S42, ESI†). According to the results from previous MD simulations, there was a notable increase in the coordination number of SO_4^{2-}. This increase suggests a reduction of free SO_4^{2-} within the electrolyte, which may potentially contribute to the observed elevation in the transference number of Zn^{2+}. Benefiting from the homoepitaxial deposition of Zn, no by-products can be found on the surface of the cycled Zn electrode (Fig. S43, ESI†). These results underscore a substantive enhancement in cycling performance achieved in the ZnF_2@Zn-IL system.

Insight into the protection mechanism of ZnF_2@Zn-IL

To shed light on the underlying mechanism of epitaxial deposition, density functional theory (DFT) calculation of the lattice electrostatic potential (Φ) was first performed,[58,59] with the Zn (002) facet serving as the model substrate. The potential fluctuation determines whether Zn atom arrival on the surface follows the atomic patterns of the substrates. Based on the TEM analysis, bare Zn exhibits prevalent lattice defects, including stacking faults, lattice tortuosity and expansion, which are categorized as line and plane defects. Additionally, vacancy defects are abundant, in particular at grain boundaries. The irregular nature of stacking faults and lattice tortuosity, normally devoid of periodicity, presents challenges for computational simulations. Consequently, we simplified the evaluation of vacancy defects' influence on the lattice potential. As shown in Fig. 5a and Fig. S44 (ESI†), the electrostatic potential distribution maps for the standard, expanded, and defective lattices were simulated, manifesting different magnitudes of electrostatic potential. The standard and expanded lattices exhibit a similar potential field distribution, while the defective lattice undergoes a drastic alteration. To quantify these changes, potential fluctuations on the different substrates along the diagonal line of the 5 × 5 supercell were plotted (Fig. 5b). On the standard lattice, the lattice potential fluctuates periodically with an amplitude of approximately 82.6 meV, which is in favor of Zn epitaxy. When the lattice expands by 15%, the amplitude of lattice potential reduces to 45.4 meV.

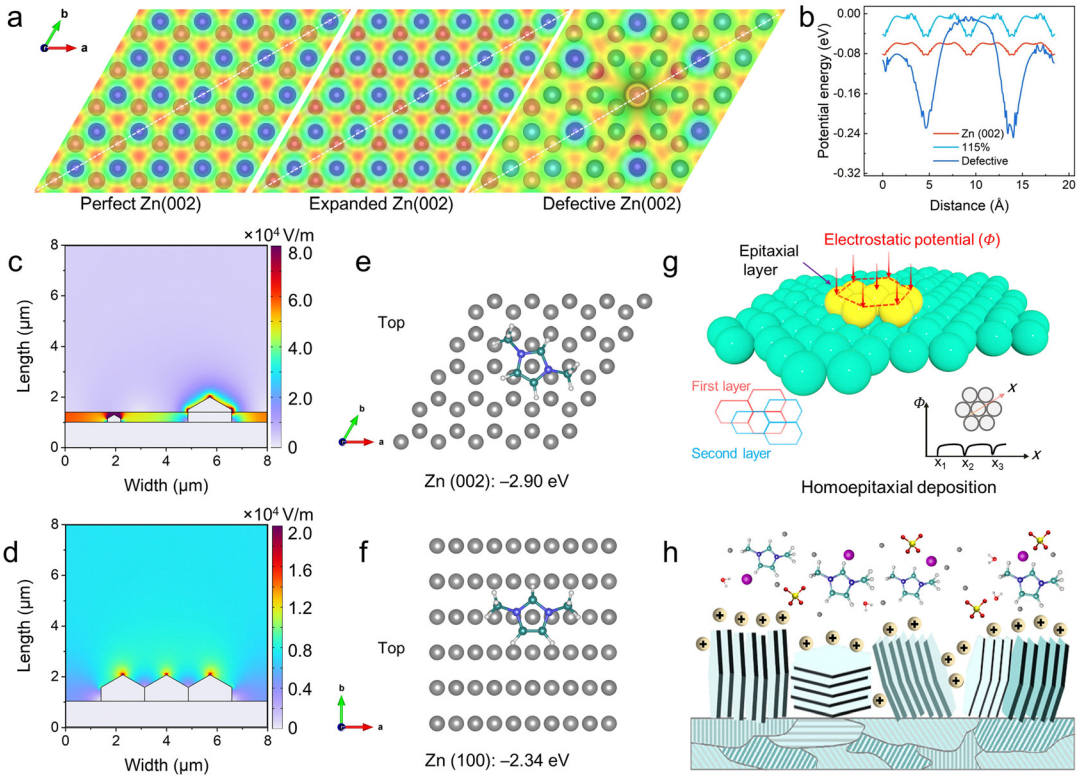

Fig. 5 Insight into the protection mechanism of the ZnF_2@Zn-IL. (a) Surface potential fluctuation maps on the standard Zn (002) lattice, the lattice expanded by 15% and the defective lattice. (b) Potential fluctuations along the lines labeled in (a). Simulated electric field distributions on the ZnF_2@Zn electrode (c) before and (d) after the detachment of ZnF_2. Adsorbed configuration of $MMIm^+$ on (e) Zn (002) and (f) Zn (101) planes. (g) Schematic diagram showing the epitaxial deposition process governed by the lattice electrostatic potential. (h) Schematic diagram of the Zn plating pattern for the ZnF_2@Zn-IL system.

This reduction in lattice potential energy diminishes the trapping ability of Zn ions during the electrodeposition process. Notably, the potential energy value reaches 247.9 meV on both sides of the defective location. The uneven potential energy landscape stemming from the randomly distributed defects at the Zn substrate would lead to Zn^{2+} accumulation at maximum potential energy sites, thus fostering dendrite formation. The calculation results reveal significant perturbations caused by small vacancies, with stacking faults and tortuosity further exacerbating these alterations.

In the context of the CVD process, the thermal-driven modification of the Zn lattice structure and the introduction of the ZnF_2 coating could be concurrently realized. To decipher the key connection between the optimized lattice structure and ZnF_2 overlayer in epitaxy, the electrodeposition morphology of the annealed Zn electrode was characterized, as shown in Fig. S45 (ESI†). The orientational landscape of deposited Zn is less pronounced than that in the ZnF_2@Zn-IL system. Its cycle lifespan is far shorter (Fig. S46, ESI†). In this sense, finite element method simulations were carried out to explore the electric field distributions on the ZnF_2 covered electrode. As for the ZnF_2@Zn, the ZnF_2 layer adheres well to the Zn surface during the initial deposition, rendering a uniformly distributed electrical field at the electrode/electrolyte interface (Fig. 5c; Fig. S47a–d, ESI†). However, with the detachment of the ZnF_2 layer, the intensification of the electric field occurs (Fig. 5d; Fig. S47e–h, ESI†), giving rise to the aggregation of Zn ions. Encouragingly, the introduced $MMIm^+$ demonstrates strong adsorption behavior on the Zn surface, as evidenced by the increased electric double-layer capacitance (Fig. S48, ESI†). The calculated adsorption energies of $MMIm^+$ on the Zn (002), (101), and (100) facets reach −2.9, −2.31, and −2.34 eV, respectively (Fig. 5e and f; Fig. S49, ESI†), suggestive of robust adsorptive effects across the typical facets. The presence of such cations on the electrode surface can effectively repel Zn ions, thereby mitigating their aggregation on the protuberances.[28,60] Both the cations and anions in the IL exert certain influences on the electrochemical performances. Particularly, the substituent group attached to cations plays a key role in tuning its adsorption behaviors on the Zn surface. The adsorption energies of imidazole cations with different substituents on Zn crystal facets were calculated (Fig. S50, ESI†). Upon meticulous comparison, it is apparent that $MMIm^+$ exhibits relatively balanced adsorption energy across three crystal facets. Therefore, $MMIm^+$ was selected as the optimal candidate. To further validate the predominant influence of $MMIm^+$ cations, an alternative IL featuring the same cation with a different anion, 1,3-dimethylimidazolium tetrafluoroborate ($MMImBF_4$), was introduced to observe the Zn deposition morphology. As depicted in Fig. S51 (ESI†), the ZnF_2@Zn substrate also demonstrates facet-governed homoepitaxial

deposition, verifying the constructive role of cations in regulating Zn deposition behaviors.

Taken together, the ZnF_2@Zn-IL system synergizes versatile pathways for stabilizing Zn anodes. The ZnF_2 overlayer intends to balance the interfacial electric field during the infancy stage, ensuring homogeneous Zn nucleation. Meanwhile, the thermal treatment of Zn *via* CVD enlarges crystal domain sizes and induces lattice structure transformation from disorder to order, establishing a more uniform lattice potential field. We deem that the lattice potential (Φ) is an important descriptor of the facet-governed Zn homoepitaxy. As foreign Zn ions approach, they gain electrons at positions with maximum (absolute value) potential energy and seamlessly merge into the intrinsic crystal lattice. For instance, crystal grains exhibiting a (002) facet, featured by a hexagonal lattice structure with ABA stacking,[61] attract Zn ions towards interstitial positions among the underlying atoms (Fig. 5g). This eventually results in the formation of hexagonal arrays. Subsequently, upon the detachment of the ZnF_2 overlayer, the adsorbed $MMIm^+$ cations on the surface of deposited Zn islands continue to play a pivotal role (Fig. 5h). These cations effectively mitigate the tip effect by repelling incoming Zn ions, thus leading to a continuous and uniform deposition of Zn. Consequently, within the same crystal grain, the Zn islands seamlessly amalgamate and form a cohesive and densely packed deposit. Therefore, the collaboration of these pathways, including the uniform nucleation induced by ZnF_2, lattice transformation driven by thermal CVD, and repulsion of Zn ions *via* $MMIm^+$ cations, contributes to the stable facet-governed Zn homoepitaxy within the ZnF_2@Zn-IL system.

AZIB full cell performance

To envisage the practical viability of ZnF_2@Zn-IL design, AZIB full cells were assembled, comprising a ZVO cathode,[2] a ZnF_2@Zn anode, and a ZS-IL electrolyte (Fig. 6a). The CV profile of the bare Zn–ZS‖ZVO cell delineates two distinct pairs of redox signals corresponding to V^{3+}/V^{4+} and V^{4+}/V^{5+} reactions (Fig. 6b). Note that a pair of new redox peaks emerge in the ZnF_2@Zn‖ZVO cell, originating from the iodine redox reaction.[62] This indicates the involvement of iodine in the electrochemical process. Fig. 6c displays the rate performances of full cells. The ZnF_2@Zn-IL system enables consistently higher capacity output as compared to its counterpart. When the current density returns to 0.5 A g^{-1}, a favorable capacity retention of 97.6% could be obtained, implying enhanced reversibility of Zn under the synergistic modulation of the ZnF_2@Zn-IL. Nyquist plots of full cells before and after cycling reveal the superior ion diffusion kinetics of the ZnF_2@Zn-IL system (Fig. S52, ESI†). In comparison with the bare Zn–ZS‖ZVO cell (Fig. S53, ESI†), the GCD profiles of the ZnF_2@Zn-IL‖ZVO cell harvest a stable charge–discharge

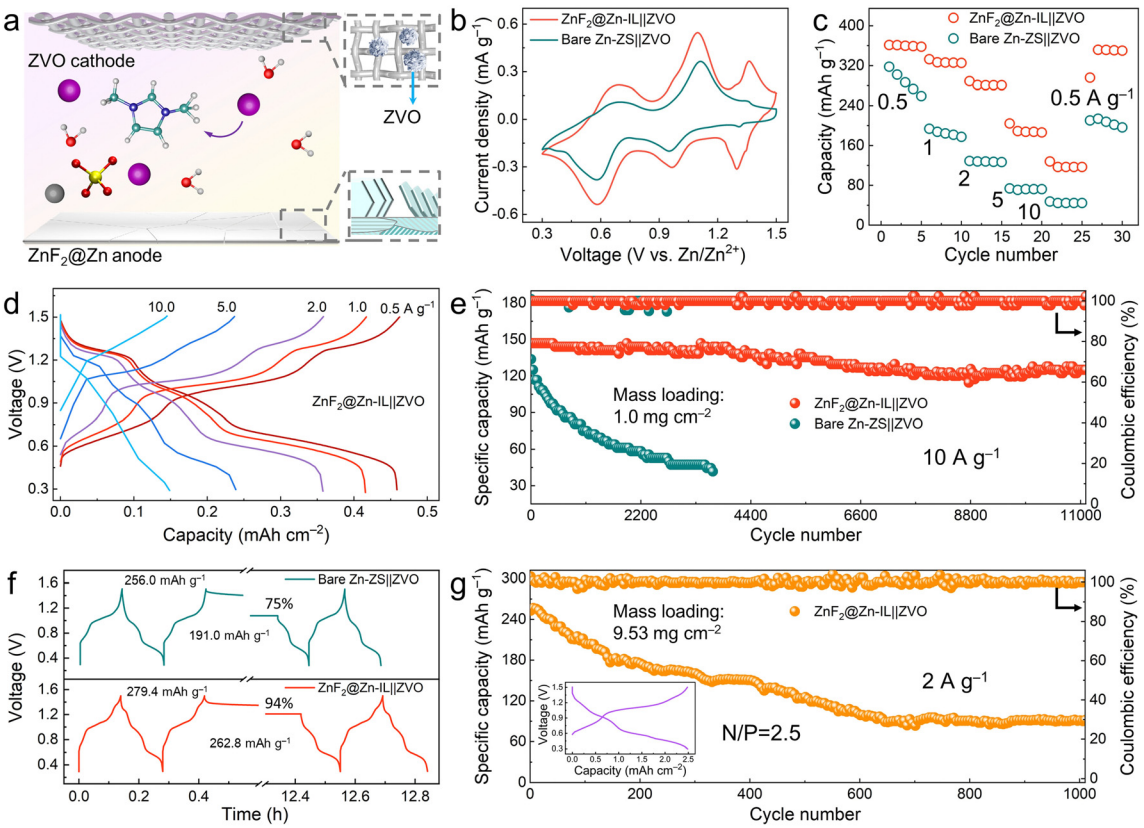

Fig. 6 Electrochemical performances of Zn‖ZVO full cells. (a) Schematic diagram of the ZnF_2@Zn-IL‖ZVO full cell. (b) CV curves for full cells at a scan rate of 0.2 mV s^{-1}. (c) Rate performances. (d) The GCD profiles of the ZnF_2@Zn-IL‖ZVO full cell. (e) Long-term cycling performances at 10.0 A g^{-1}. (f) GCD curves with a resting time of 12 h. (g) Long-term cycling performances with a mass loading of 9.53 mg cm^{-2} and a N/P ratio of 2.5.

platform at ~1.2 V (Fig. 6d), which might be ascribed to the redox reaction between I^- and I_2.[63,64] This newly established discharge platform not only elevates the discharge voltage of the battery but also augments its overall capacity. As expected, the ZnF_2@Zn-IL‖ZVO cell exhibits a higher initial capacity of 146.9 mA h g^{-1} as compared to the Zn–ZS‖ZVO cell (133.7 mA h g^{-1}). It sustains at 125 mA h g^{-1} even after 11 000 cycles at 10.0 A g^{-1} (Fig. 6e),[65,66] which surpasses the cycling performances of most recently reported full batteries (Table S4, ESI†). In stark contrast, the bare Zn–ZS‖ZVO cell experiences a rapid capacity decay within 1000 cycles, a consequence of rampant dendrite growth and undesirable side reactions. The Zn anode after 10 000 cycles still displays an epitaxial deposition morphology inside a single grain (Fig. S54, ESI†). Such an epitaxial growth mitigates dendritic proliferation and detrimental reaction, contributing to the overall stability and longevity of the full cell. Moreover, I_3^- tends to react with dead Zn during cycling, leading to the regeneration of Zn^{2+}.[67] At the same time, iodine exhibits recyclability in the electrochemical process, as evidenced by the obvious charging/discharging platforms observed after 7000 cycles (Fig. S55, ESI†). Hence, iodine effectively acts as a mediator in the electrochemical processes,[66,68] facilitating the reversible cycling of Zn. Moreover, the capacity retention rate during shelving is a critical performance metric for a full cell. As shown in Fig. 6f, it is evident that the full cell utilizing ZnF_2@Zn-IL maintains 94% of its original capacity after resting for 12 h, while its counterpart encounters a decrease to 75% in capacity retention. This indicates that the incorporation of ZnF_2@Zn-IL could effectively prevent the Zn anode from noticeable self-discharge. The feasibility of the ZnF_2@Zn-IL system under low negative-to-positive capacity ratio (N/P ratio) conditions was in target validated using high-loading cathodes (9.53 mg cm^{-2}) and thin Zn foils (10 μm). Impressively, the assembled ZnF_2@Zn-IL‖ZVO full cell is able to endure 1000 cycles at 2.0 A g^{-1} with a low N/P ratio of 2.5 (Fig. 6g), showcasing the application potential in practical electrochemical devices. These results collectively confirm that ZnF_2@Zn-IL can guide epitaxial Zn deposition and suppress parasitic reactions at the anode/electrolyte interface, ultimately in favor of elevating the reversibility and durability of AZIBs.

Conclusions

In summary, we have developed a synchronized strategy involving interfacial layer construction and electrolyte additive modulation to co-regulate stable homoepitaxial Zn electrodeposition. The CVD design of ZnF_2@Zn plays a key role in optimizing crystallinity within the Zn foil, rendering a periodic lattice potential field that is conducive to epitaxial deposition of Zn. Meanwhile, the overlayer grown on the surface, together with the ionic liquid additives, markedly enhances the uniformity of Zn^{2+} transport and deposition. Such a strategy not only ensures a dendrite-free Zn anode but also regulates the solvation structure and inhibits hydrogen evolution. Exhaustive characterization studies have unveiled the discernible correlation between epitaxial deposition and the crystal lattice structure. As a result, both the symmetric and full cells based on the ZnF_2@Zn-IL demonstrate favorable cycling stability across a wide range of testing conditions. Our findings offer a comprehensive understanding of Zn deposition mechanisms, showcasing the possibility of the facet-governed methodology in enhancing the stability of Zn anodes. The realization of homoepitaxy on polycrystalline Zn offers valuable insights into advanced electrode/electrolyte design, paving the way for pragmatic AZIBs.

Data availability

The data supporting this article have been included as part of the ESI.†

Author contributions

J. S., Z. G. and X. Y. designed the concept. X. Y. prepared and characterized the ZnF_2@Zn-IL system. X. Y., Z. C., Y. S., and Y. Z. performed the electrochemical test and explored the protective mechanism. Y. L. conducted the DFT calculation. Z. L. and P. G. carried out the TEM characterization. H. J. conducted the MD simulations, and J. P. performed the finite element analysis. X. Y., C. W., S. D., Z. G. and J. S. co-wrote the manuscript. All authors discussed the experimental and theoretical results and commented on the manuscript. All authors have approved the final version of the manuscript.

Conflicts of interest

The authors declare no competing interests.

Acknowledgements

This work was supported by the National Key R&D Program of China (2019YFA0708201), the National Natural Science Foundation of China (22179089, T2188101, and 52302289), and the Science Fund for Distinguished Young Scholars of Jiangsu Province (BK20211503). The authors also acknowledge support from the Suzhou Key Laboratory for Advanced Carbon Materials and Wearable Energy Technologies, Suzhou, China. J. P. acknowledges the use of the computational infrastructure of the research group of Prof. Robert H. Blick (CHyN, Unversität Hamburg).

References

1 J. Zheng and L. A. Archer, *Sci. Adv.*, 2021, **7**, eabe0219.
2 X. Yang, W. Li, Z. Chen, M. Tian, J. Peng, J. Luo, Y. Su, Y. Zou, G. Weng, Y. Shao, S. Dou and J. Sun, *Angew. Chem., Int. Ed.*, 2023, **62**, e202218454.
3 X. Yang, J. Lv, C. Cheng, Z. Shi, J. Peng, Z. Chen, X. Lian, W. Li, Y. Zou, Y. Zhao, M. H. Rummeli, S. Dou and J. Sun, *Adv. Sci.*, 2023, **10**, 2206077.

4 X. Y. Yu, Z. G. Li, X. H. Wu, H. T. Zhang, Q. G. Zhao, H. F. Liang, H. Wang, D. L. Chao, F. Wang, Y. Qiao, H. S. Zhou and S. G. Sun, *Joule*, 2023, **7**, 1145–1175.
5 Q. Yang, Q. Li, Z. Liu, D. Wang, Y. Guo, X. Li, Y. Tang, H. Li, B. Dong and C. Zhi, *Adv. Mater.*, 2020, **32**, 2001854.
6 P. Sun, L. Ma, W. Zhou, M. Qiu, Z. Wang, D. Chao and W. Mai, *Angew. Chem., Int. Ed.*, 2021, **60**, 18247–18255.
7 Q. Zhang, Y. Su, Z. Shi, X. Yang and J. Sun, *Small*, 2022, **18**, 2203583.
8 T. C. Li, Y. Lim, X. L. Li, S. Luo, C. Lin, D. Fang, S. Xia, Y. Wang and H. Y. Yang, *Adv. Energy Mater.*, 2022, **12**, 2103231.
9 Y. Su, B. Liu, Q. Zhang, J. Peng, C. Wei, S. Li, W. Li, Z. Xue, X. Yang and J. Sun, *Adv. Funct. Mater.*, 2022, **32**, 2204306.
10 Y. Su, B. Chen, Y. Sun, Z. Xue, Y. Zou, D. Yang, L. Sun, X. Yang, C. Li, Y. Yang, X. Song, W. Guo, S. Dou, D. Chao, Z. Liu and J. Sun, *Adv. Mater.*, 2023, **35**, 2301410.
11 G. Weng, Z. Dong, P. Xiang, Y. Zhu, C. Wu, X. Yang, H. Liu and S. Dou, *Adv. Funct. Mater.*, 2024, **34**, 2400839.
12 X. Yang, C. Li, Z. Sun, S. Yang, Z. Shi, R. Huang, B. Liu, S. Li, Y. Wu, M. Wang, Y. Su, S. Dou and J. Sun, *Adv. Mater.*, 2021, **33**, 2105951.
13 Y. Zou, X. Yang, L. Shen, Y. Su, Z. Chen, X. Gao, J. Zhou and J. Sun, *Energy Environ. Sci.*, 2022, **15**, 5017–5038.
14 X. Yang, Z. Dong, G. Weng, Y. Su, J. Huang, H. Chai, Y. Zhang, K. Wu, J. B. Baek, J. Sun, D. Chao, H. Liu, S. Dou and C. Wu, *Adv. Energy Mater.*, 2024, **14**, 2401293.
15 J. Zheng, Q. Zhao, T. Tang, J. Yin, C. D. Quilty, G. D. Renderos, X. Liu, Y. Deng, L. Wang, D. C. Bock, C. Jaye, D. Zhang, E. S. Takeuchi, K. J. Takeuchi, A. C. Marschilok and L. A. Archer, *Science*, 2019, **366**, 645–648.
16 Z. Zhao, R. Wang, C. Peng, W. Chen, T. Wu, B. Hu, W. Weng, Y. Yao, J. Zeng, Z. Chen, P. Liu, Y. Liu, G. Li, J. Guo, H. Lu and Z. Guo, *Nat. Commun.*, 2021, **12**, 6606.
17 Z. Chen, Q. Wu, X. Han, C. Wang, J. Chen, T. Hu, Q. He, X. Zhu, D. Yuan, J. Chen, Y. Zhang, L. Yang, Y. Ma and J. Zhao, *Angew. Chem., Int. Ed.*, 2024, **63**, e202401507.
18 W. D. Zhang, Q. Zhao, Y. P. Hou, Z. Y. Shen, L. Fan, S. D. Zhou, Y. Y. Lu and L. A. Archer, *Sci. Adv.*, 2021, **7**, eabl3752.
19 Z. Liu, Z. Guo, L. Fan, C. Zhao, A. Chen, M. Wang, M. Li, X. Lu, J. Zhang, Y. Zhang and N. Zhang, *Adv. Mater.*, 2024, **36**, 2305988.
20 L. Ren, Z. Hu, C. Peng, L. Zhang, N. Wang, F. Wang, Y. Xia, S. Zhang, E. Hu and J. Luo, *Proc. Natl. Acad. Sci. U. S. A.*, 2024, **121**, e2309981121.
21 S. D. Pu, C. Gong, Y. T. Tang, Z. Ning, J. Liu, S. Zhang, Y. Yuan, D. Melvin, S. Yang, L. Pi, J.-J. Marie, B. Hu, M. Jenkins, Z. Li, B. Liu, S. C. E. Tsang, T. J. Marrow, R. C. Reed, X. Gao, P. G. Bruce and A. W. Robertson, *Adv. Mater.*, 2022, **34**, 2202552.
22 G. Liang, J. Zhu, B. Yan, Q. Li, A. Chen, Z. Chen, X. Wang, B. Xiong, J. Fan, J. Xu and C. Zhi, *Energy Environ. Sci.*, 2022, **15**, 1086–1096.
23 J. Han, H. Euchner, M. Kuenzel, S. M. Hosseini, A. Groß, A. Varzi and S. Passerini, *ACS Energy Lett.*, 2021, **6**, 3063–3071.
24 J. Zheng, Y. Deng, J. Yin, T. Tang, R. Garcia-Mendez, Q. Zhao and L. A. Archer, *Adv. Mater.*, 2022, **34**, 2106867.
25 Y. Zhao, S. Guo, M. Chen, B. Lu, X. Zhang, S. Liang and J. Zhou, *Nat. Commun.*, 2023, **14**, 7080.
26 C. L. Xie, S. F. Liu, Z. F. Yang, H. M. Ji, S. H. Zhou, H. Wu, C. Hu, Y. G. Tang, X. B. Ji, Q. Zhang and H. Y. Wang, *Angew. Chem., Int. Ed.*, 2023, **62**, e202218612.
27 H. Zhang, Y. Zhong, J. Li, Y. Liao, J. Zeng, Y. Shen, L. Yuan, Z. Li and Y. Huang, *Adv. Energy Mater.*, 2022, **13**, 2203254.
28 L. Yu, J. Huang, S. Wang, L. Qi, S. Wang and C. Chen, *Adv. Mater.*, 2023, **35**, 2210789.
29 M. Zhao, J. F. Rong, F. Huo, Y. Q. Lv, B. W. Yue, Y. Xiao, Y. Chen, G. L. Hou, J. S. Qiu and S. M. Chen, *Adv. Mater.*, 2022, **34**, 2203153.
30 X. Zhao, Y. Wang, C. Huang, Y. Gao, M. Huang, Y. Ding, X. Wang, Z. Si, D. Zhou and F. Kang, *Angew. Chem., Int. Ed.*, 2023, **62**, e202312193.
31 J. Zhang, W. Huang, L. Li, C. Chang, K. Yang, L. Gao and X. Pu, *Adv. Mater.*, 2023, **35**, 2300073.
32 T. Li, W. Guo, L. Ma, W. Li, Z. Yu, Z. Han, S. Gao, L. Liu, D. Fan, Z. Wang, Y. Yang, W. Lin, Z. Luo, X. Chen, N. Dai, X. Tu, D. Pan, Y. Yao, P. Wang, Y. Nie, J. Wang, Y. Shi and X. Wang, *Nat. Nanotechnol.*, 2021, **16**, 1201–1207.
33 T. A. Chen, C. P. Chuu, C. C. Tseng, C. K. Wen, H. S. P. Wong, S. Y. Pan, R. T. Li, T. A. Chao, W. C. Chueh, Y. F. Zhang, Q. Fu, B. I. Yakobson, W. H. Chang and L. J. Li, *Nature*, 2020, **579**, 219–223.
34 X. Xie, S. Liang, J. Gao, S. Guo, J. Guo, C. Wang, G. Xu, X. Wu, G. Chen and J. Zhou, *Energy Environ. Sci.*, 2020, **13**, 503–510.
35 R. Huang, J. W. Zhang, W. Wang, X. H. Wu, X. L. Liao, T. T. Lu, Y. Z. Li, J. L. Chen, S. Chen, Y. Qiao, Q. Zhao and H. Wang, *Energy Environ. Sci.*, 2024, **17**, 3179–3190.
36 R. Zhao, X. Dong, P. Liang, H. Li, T. Zhang, W. Zhou, B. Wang, Z. Yang, X. Wang, L. Wang, Z. Sun, F. Bu, Z. Zhao, W. Li, D. Zhao and D. Chao, *Adv. Mater.*, 2023, **35**, 2209288.
37 L. Wang, B. Zhang, W. Zhou, Z. Zhao, X. Liu, R. Zhao, Z. Sun, H. Li, X. Wang, T. Zhang, H. Jin, W. Li, A. Elzatahry, Y. Hassan, H. J. Fan, D. Zhao and D. Chao, *J. Am. Chem. Soc.*, 2024, **146**, 6199–6208.
38 Z. Y. Zhang, Y. F. Zhang, M. H. Ye, Z. P. Wen, Y. C. Tang, X. Q. Liu and C. C. Li, *Angew. Chem., Int. Ed.*, 2023, **62**, e202311032.
39 S. Zhao, Y. Zhang, J. Li, L. Qi, Y. Tang, J. Zhu, J. Zhi and F. Huang, *Adv. Mater.*, 2023, **35**, 2300195.
40 Z. Zhao, J. Lai, D. T. Ho, Y. Lei, J. Yin, L. Chen, U. Schwingenschloegl and H. N. Alshareef, *ACS Energy Lett.*, 2022, **8**, 608–618.
41 S. Zheng, L. Wei, Z. Zhang, J. Pan, J. He, L. Gao and C. C. Li, *Nano Lett.*, 2022, **22**, 9062–9070.
42 L. T. Ma, S. M. Chen, N. Li, Z. X. Liu, Z. J. Tang, J. A. Zapien, S. M. Chen, J. Fan and C. Y. Zhi, *Adv. Mater.*, 2020, **32**, 1908121.
43 D. Lee, H.-I. Kim, W.-Y. Kim, S.-K. Cho, K. Baek, K. Jeong, D. B. Ahn, S. Park, S. J. Kang and S.-Y. Lee, *Adv. Funct. Mater.*, 2021, **31**, 2103850.
44 R. Chen, Q. Liu, L. Xu, X. Zuo, F. Liu, J. Zhang, X. Zhou and L. Mai, *ACS Energy Lett.*, 2022, **7**, 1719–1727.

45 F. Ilyas, J. H. Chen, Y. Zhang, Y. D. Huang, H. Y. Ma and J. L. Wang, *Energy Storage Mater.*, 2023, **55**, 566–574.
46 X. Y. Nie, L. C. Miao, W. T. Yuan, G. Q. Ma, S. L. Di, Y. Y. Wang, S. G. Shen and N. Zhang, *Adv. Funct. Mater.*, 2022, **32**, 2203905.
47 Q. Zhang, Y. Ma, Y. Lu, X. Zhou, L. Lin, L. Li, Z. Yan, Q. Zhao, K. Zhang and J. Chen, *Angew. Chem., Int. Ed.*, 2021, **60**, 23357–23364.
48 Y. Yang, C. Y. Liu, Z. H. Lv, H. Yang, Y. F. Zhang, M. H. Ye, L. B. Chen, J. B. Zhao and C. C. Li, *Adv. Mater.*, 2021, **33**, 2007388.
49 L. Ma, Q. Li, Y. Ying, F. Ma, S. Chen, Y. Li, H. Huang and C. Zhi, *Adv. Mater.*, 2021, **33**, 2007406.
50 L. Cao, D. Li, T. Pollard, T. Deng, B. Zhang, C. Yang, L. Chen, J. Vatamanu, E. Hu, M. J. Hourwitz, L. Ma, M. Ding, Q. Li, S. Hou, K. Gaskell, J. T. Fourkas, X.-Q. Yang, K. Xu, O. Borodin and C. Wang, *Nat. Nanotechnol.*, 2021, **16**, 902–910.
51 Y. W. Zhao, H. Hong, L. H. Zhong, J. X. Zhu, Y. Hou, S. P. Wang, H. M. Lv, P. Liang, Y. Guo, D. H. Wang, P. Li, Y. X. Wang, Q. Li, S. C. Cao, H. F. Li and C. Y. Zhi, *Adv. Energy Mater.*, 2023, **13**, 2300627.
52 D. Li, L. S. Cao, T. Deng, S. F. Liu and C. S. Wang, *Angew. Chem., Int. Ed.*, 2021, **60**, 13035–13041.
53 Y. Chu, S. Zhang, S. Wu, Z. Hu, G. Cui and J. Luo, *Energy Environ. Sci.*, 2021, **14**, 3609–3620.
54 S. L. Di, X. Y. Nie, G. Q. Ma, W. T. Yuan, Y. Y. Wang, Y. C. Liu, S. G. Shen and N. Zhang, *Energy Storage Mater.*, 2021, **43**, 375–382.
55 S. Liu, J. Mao, W. K. Pang, J. Vongsvivut, X. Zeng, L. Thomsen, Y. Wang, J. Liu, D. Li and Z. Guo, *Adv. Funct. Mater.*, 2021, **31**, 2104281.
56 S. Wu, S. Zhang, Y. Z. Chu, Z. L. Hu and J. Y. Luo, *Adv. Funct. Mater.*, 2021, **31**, 2107397.
57 C. Cui, D. Han, H. Lu, Z. Li, K. Zhang, B. Zhang, X. Guo, R. Sun, X. Ye, J. Gao, Y. Liu, Y. Guo, R. Meng, C. Wei, L. Yin, F. Kang, Z. Weng and Q.-H. Yang, *Adv. Energy Mater.*, 2023, **13**, 2301466.
58 W. Kong, H. Li, K. Qiao, Y. Kim, K. Lee, Y. Nie, D. Lee, T. Osadchy, R. J. Molnar, D. K. Gaskill, R. L. Myers-Ward, K. M. Daniels, Y. Zhang, S. Sundram, Y. Yu, S.-h Bae, S. Rajan, Y. Shao-Horn, K. Cho, A. Ougazzaden, J. C. Grossman and J. Kim, *Nat. Mater.*, 2018, **17**, 999–1004.
59 B. Liu, Q. Chen, Z. Chen, S. Yang, J. Shan, Z. Liu, Y. Yin, F. Ren, S. Zhang, R. Wang, M. Wu, R. Hou, T. Wei, J. Wang, J. Sun, J. Li, Z. Liu, Z. Liu and P. Gao, *Nano Lett.*, 2022, **22**, 3364–3371.
60 J. Xu, H. Li, Y. Jin, D. Zhou, B. Sun, M. Armand and G. Wang, *Adv. Mater.*, 2023, **36**, 2309726.
61 A. Yacoby, *Nat. Phys.*, 2011, **7**, 925–926.
62 Q. Zhang, Y. Ma, Y. Lu, Y. Ni, L. Lin, Z. Hao, Z. Yan, Q. Zhao and J. Chen, *J. Am. Chem. Soc.*, 2022, **144**, 18435–18443.
63 S.-J. Zhang, J. Hao, H. Li, P.-F. Zhang, Z.-W. Yin, Y.-Y. Li, B. Zhang, Z. Lin and S.-Z. Qiao, *Adv. Mater.*, 2022, **34**, 2201716.
64 Y. Lyu, J. A. Yuwono, P. Wang, Y. Wang, F. Yang, S. Liu, S. Zhang, B. Wang, K. Davey, J. Mao and Z. Guo, *Angew. Chem., Int. Ed.*, 2023, **62**, e202303011.
65 J. F. Lei, Y. X. Yao, Z. Y. Wang and Y. C. Lu, *Energy Environ. Sci.*, 2021, **14**, 4418–4426.
66 C. Jin, T. Liu, O. Sheng, M. Li, T. Liu, Y. Yuan, J. Nai, Z. Ju, W. Zhang, Y. Liu, Y. Wang, Z. Lin, J. Lu and X. Tao, *Nat. Energy*, 2021, **6**, 378–387.
67 H. Chen, X. Li, K. Fang, H. Wang, J. Ning and Y. Hu, *Adv. Energy Mater.*, 2023, **13**, 2302187.
68 M. Cui, N. Ma, H. Lei, Y. Liu, W. Ling, S. Chen, J. Wang, H. Li, Z. Li, J. Fan and Y. Huang, *Angew. Chem., Int. Ed.*, 2023, **62**, e202303845.